Figure 4.12: Early stage dynamics involving 7933 neurons. For each cell, electrical synapses exist among nearest-neighbour neurons and the chemical ones are 75% of links among cells belonging to a circle having radius 1/16. The whole network is initially at rest but, after a while, a continuum external current $I = 0.1$ is applied to 319 of them randomly chosen. In the second frame, neurons which receive the injected current become apparent. In the third snapshot, a propagating phenomenon arises

where, with respect to (4.6), we write $f(v,r) = \hat{f}(v,r) + I$, so that

$$\hat{f}(v,r) = -v(v-a)(v-1)-r, \qquad g(v,r) = bv-cr, \qquad I = I(x,t) \text{ (an applied current).}$$

In particular we will discuss the existence and uniqueness of solution of the corresponding initial-boundary value problem up to any final $T_F > 0$. We will also prove that the solution stays bounded for all times.

4.3.1 Mathematical formulation

We assume that the region occupied by the neurons is a bounded open connected set $\Omega \subset \mathbb{R}^m$, with $m = 1, 2,$ or 3. Let $u = (v,r,s)^T$ be the vector collecting the three unknowns, i.e., $u(x,t) = (v(x,t), r(x,t), s(x,t))^T$. We are interested in solving (4.9) from time $t_0 = 0$ to some T_F, so we think u as defined in $\bar{\Omega} \times [0, T_F]$ with values in $\mathbb{R}^3$. For any fixed $t \in [0, T_F]$, $u(t)$ will denote the function $u(\cdot, t) : \bar{\Omega} \to \mathbb{R}^3$.

It is convenient to introduce the function
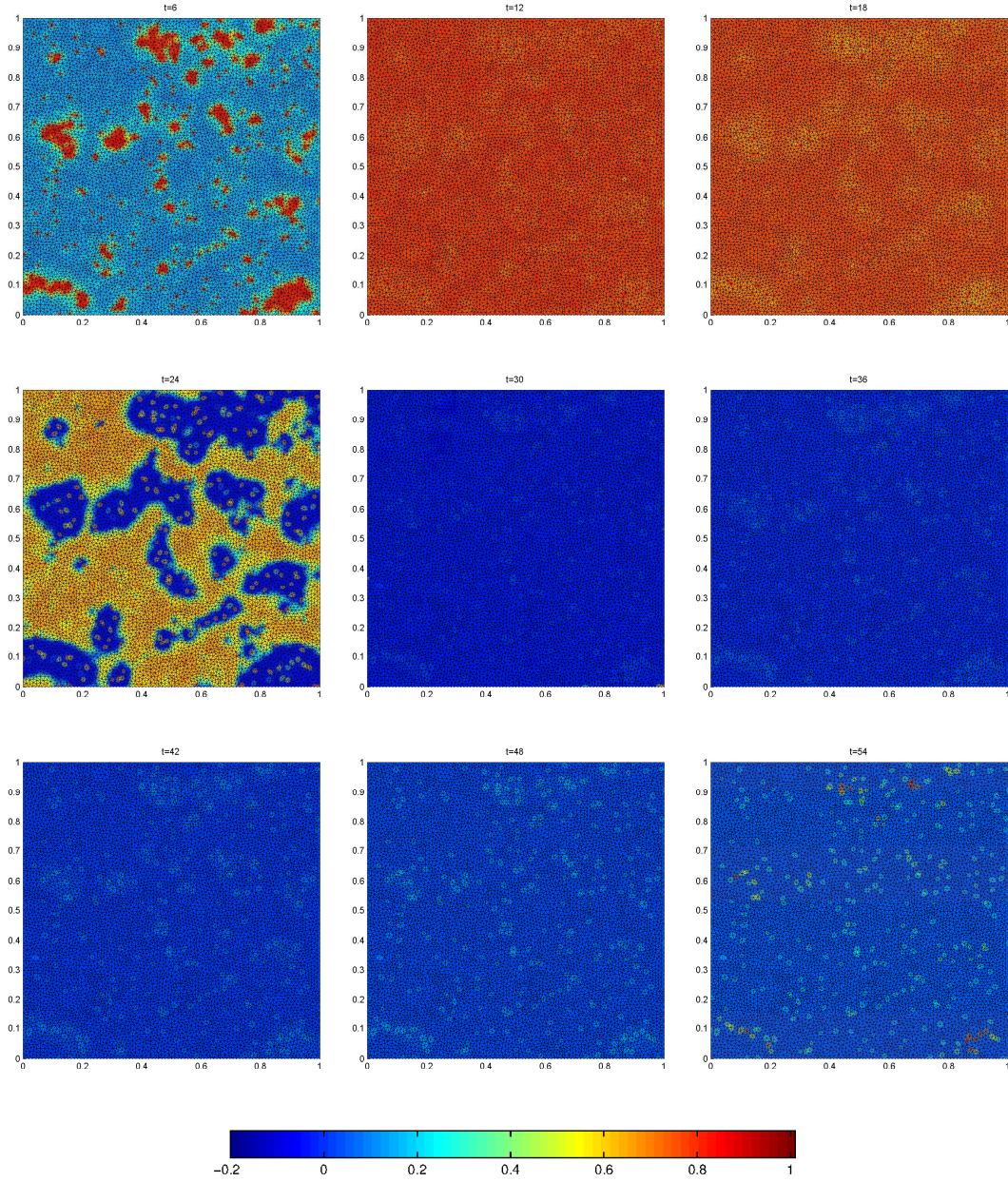
$$h(v,s) := \alpha H_\infty(v - v_T)(1 - s) ,$$

102

Figure 4.13: Snapshots concerning the evolution of the solution represented in Figure 4.12. In particular, the synchronous excitation phenomenon is shown. The evolution of this dynamics is depicted in Figure 4.14
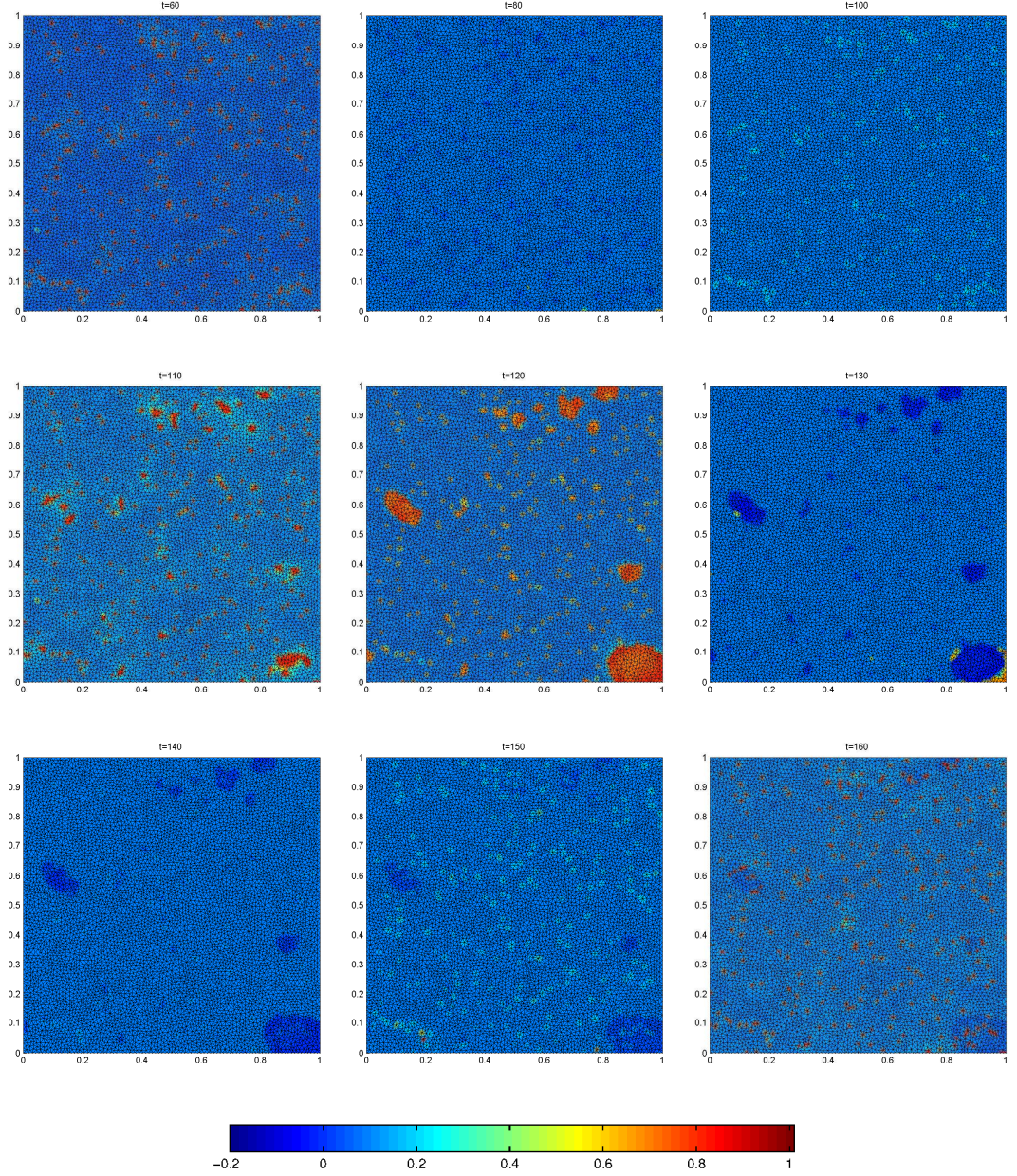
103

Figure 4.14: Final stages of the solution exhibited in Figure 4.12-4.13. In contrast to what happens in Figure 4.11 no new excitatory synchronous events appear. It is due to the strong inhibition selected by imposing $v_{\text{syn}}^{I} = -0.9$ to the inhibitory neurons, which energetically discourages the propagation of the excitation

and the operator $K(v, s)$ defined as

$$[K(v, s)](x, t) := -g_{\mathrm{syn}} \left(\int_{y \in \mathcal{B}(x)} w(x, y) s(y, t) (v(x, t) - v_{\mathrm{syn}}(y)) \, \mathrm{d}y \right) .$$

Thus, (4.9) can be written as

$$\begin{aligned} \frac{\partial v}{\partial t} - d^* \Delta v &= \hat{f}(v, r) + K(v, s) + I \\ \frac{\partial r}{\partial t} + cr &= bv , \\ \frac{\partial s}{\partial t} + \beta s &= h(v, s) , \end{aligned} \qquad (4.10)$$

i.e., introducing the linear operator $Au = (-d^* \Delta v, cr, \beta s)^T$ and the nonlinear operator $F(u) = (\hat{f}(v, r) + K(v, s), bv, h(v, s))^T$, and setting $\mathcal{I} = (I, 0, 0)^T$, we write the system in vector form as

$$\frac{\partial u}{\partial t} + Au = F(u) + \mathcal{I} . \qquad (4.11)$$

The system has to be supplemented by an initial condition

$$u(0) = u_0, \text{ i.e., } u(x, 0) = u_0(x) = (v_0(x), r_0(x), s_0(x))^T . \qquad (4.12)$$

Furthermore, the presence of the diffusion operator $-d^* \Delta$ applied to the potential v calls for a boundary condition for this variable. We assume that v is prescribed at the boundary $\partial \Omega$ for all times (Dirichlet boundary conditions); applying a suitable change of unknown, it is actually not restrictive to assume that $v = 0$ on $\partial \Omega \times [0, T_F]$. Obviously, other boundary conditions could be enforced instead, such as the periodicity conditions already used in $\Omega = \mathcal{B}$ in previous chapters.

Recalling the weak formulation of the heat equation submitted to homogeneous Dirichlet boundary conditions, we introduce the Sobolev space $H_0^1(\Omega) = \{v \in L^2(\Omega) : \nabla v \in (L^2(\Omega))^m$ (in the sense of distributions) and $v = 0$ on $\partial \Omega\}$ equipped with the norm $\|v\|_{H_0^1(\Omega)} = \|\nabla v\|_{(L^2(\Omega))^m}$, and we define the Hilbert space

$$V := H_0^1(\Omega) \times L^2(\Omega) \times L^2(\Omega)$$

equipped with the product norm

$$\|u\|_V := \left(\|v\|_{H_0^1(\Omega)}^2 + \|r\|_{L^2(\Omega)}^2 + \|s\|_{L^2(\Omega)}^2 \right)^{1/2} .$$

We will also set

$$H := L^2(\Omega) \times L^2(\Omega) \times L^2(\Omega) \,,$$

which we identify with its dual H' via the Riesz operator; consequently, the dual of V is

$$V' = H^{-1}(\Omega) \times L^2(\Omega) \times L^2(\Omega) \,,$$

where $H^{-1}(\Omega)$ denotes the dual of $H_0^1(\Omega)$. It is well known that the operator $-\Delta$ is an isomorphism between $H_0^1(\Omega)$ and $H^{-1}(\Omega)$; therefore,

$$A : V \to V'$$

is an isomorphism, too (since by assumption $d^* > 0$, $c > 0$, $\beta > 0$). In particular, the following coercivity inequality holds: setting $\gamma := \min(d^*, c, \beta)$ one has

$$\langle Av, v \rangle \geq \gamma \|v\|_V^2 \qquad \text{for all } v \in V \,, \tag{4.13}$$

where $\langle \cdot, \cdot \rangle$ denotes the duality pairing between $H^{-1}(\Omega)$ and $H_0^1(\Omega)$.

Concerning the nonlinear operator F, we have the following properties. The term $\hat{f}(v, r)$ behaves like $-v^3 - r$ for large $|v|$; thus, thanks to the embedding $H^1(\Omega) \subset L^6(\Omega)$ for $m \leq 6$, we have

$$\|\hat{f}(v, r)\|_{L^2(\Omega)} \leq C_1 \|v\|_{H_0^1(\Omega)}^3 + \|r\|_{L^2(\Omega)}$$

provided $v \in H^1(\Omega)$ and $r \in L^2(\Omega)$. On the other hand, for the term $K(v, s)$ we observe that the weights $w(x, y)$ are uniformly bounded in $\Omega \times \Omega$, so that a.e. in Ω one has

$$
\begin{aligned}
|[K(v, s)](x)| \;\leq\; & g_{\text{syn}} \left(\left| \int_{y \in \mathcal{B}(x)} w(x, y) s(y, t) \, \mathrm{d}y \right| |v(x)| + \right. \\
& \left. + \left| \int_{y \in \mathcal{B}(x)} w(x, y) s(y, t) v_{\text{syn}}(y) \, \mathrm{d}y \right| \right) \\
\;\leq\; & C_2 \|s\|_{L^2(\Omega)} \left(|v(x)| + \|v_{\text{syn}}\|_{L^2(\Omega)} \right) \,,
\end{aligned}
$$

whence

$$\|K(v, s)\|_{L^2(\Omega)} \leq C_3 \|s\|_{L^2(\Omega)} \left(\|v\|_{L^2(\Omega)} + \|v_{\text{syn}}\|_{L^2(\Omega)} \right) \,,$$

provided v, v_{syn} and s belong to $L^2(\Omega)$. Finally, we obviously have $\|h(v, s)\|_{L^2(\Omega)} \leq C_4 \|s\|_{L^2(\Omega)} + C_5$ if $s \in L^2(\Omega)$. Summarizing, the nonlinear term $F(u)$ belongs to H whenever $u \in V$.

This proves that if (4.9) admits at time t a solution $u(t) \in V$, and if $I(t) \in L^2(\Omega)$, then $\frac{\partial u}{\partial t}(t) = -Au(t) + F(u(t)) + \mathcal{I}(t) \in V'$. Furthermore, if we assume that $u \in L^2(0, T_F; V)$ with its first component $v \in L^6(0, T_F; H_0^1(\Omega))$, and if the external current I satisfies $I \in L^2(0, T_F; L^2(\Omega))$, then $Au \in L^2(0, T_F; V')$ and $F(u)$, $\mathcal{I} \in L^2(0, T_F; H) \subset L^2(0, T_F; V')$, hence, from equation (4.11) we deduce that $\frac{\partial u}{\partial t} \in L^2(0, T_F; V')$. This implies $u \in C^0([0, T_F]; H)$, hence, the initial value $u(0)$ is well-defined in H, and we are let to assume the initial datum $u_0 \in H$.

In conclusion, we consider the following

Mathematical formulation of model (4.9). *Given $u_0 \in H$, $v_{\mathrm{syn}} \in L^2(\Omega)$ and $I \in L^2(0, T_F; L^2(\Omega))$, we look for $u \in L^2(0, T_F; V) \cap C^0([0, T_F]; H)$ with its first component $v \in L^6(0, T_F; H_0^1(\Omega))$ such that $u(0) = u_0$ and*

$$\frac{\partial u}{\partial t} + Au = F(u) + \mathcal{I} \qquad \text{in } L^2(0, T_F; V') . \tag{4.14}$$

4.3.2 Regularized problem

The mapping F is not continuous in the third component, due to the presence of the Heaviside function H_∞; indeed, the third equation in (4.10) is an instance of a differential equation with discontinuous righthand side (see [16] where ordinary differential equations are treated; our situation is a bit more complex, due to the dependence of all functions on the spatial variable x as well). On the other hand, the first component of F is locally but not globally Lipschitz continuous, due to the presence of algebraic nonlinearities. Therefore, we proceed by regularizing and approximating F, in order to get a family of problems which admit existence and uniqueness of the solution; next, we will discuss the limit behaviour of this family.

Given any constant $M > 0$, let $\chi_M : \mathbb{R} \to \mathbb{R}$ be the cut-off function

$$\chi_M(z) = \begin{cases} z & \text{if } |z| \leq M, \\ M\dfrac{z}{|z|} & \text{if } |z| > M, \end{cases}$$

and let $\chi_M(\varphi)$ denote its composition $\chi_M \circ \varphi$ with a real function φ. We modify the right-hand side of the first equation in (4.10) by replacing $\hat{f}(v, r)$ by $\hat{f}_M(v, r) := \hat{f}(\chi_M(v), r)$, and $K(v, s)$ by $K_M(v, s) := K(\chi_M(v), \chi_M(s))$.

On the other hand, given any constant $L > 0$, let $H_L : \mathbb{R} \to \mathbb{R}$ denote the regularized

Heaviside function, defined as

$$H_L(z) = \begin{cases} 0 & \text{if } z \leq 0, \\ Lz & \text{if } 0 < z < 1/L, \\ 1 & \text{if } z \geq 1/L, \end{cases}$$

which is Lipschitz-continuous with Lipschitz constant L and pointwise converges to the Heaviside function H_∞ as $L \to \infty$. We modify the right-hand side of the third equation in (4.10) by replacing $h(v,s)$ by $h_{M,L}(v,s) := \alpha H_L(v - v_T)(1 - \chi_M(s))$.

In conclusion, we introduce the nonlinear operator

$$F_{M,L}(u) := (\hat{f}_M(v,r) + K_M(v,s), bv, h_{M,L}(v,s))^T$$

and we easily note that

$$\|F_{M,L}(u)\|_H \leq C_1\|v\|_{L^2(\Omega)} + C_2\|r\|_{L^2(\Omega)} + C_3\|s\|_{L^2(\Omega)} + C_4$$

for suitable constants $C_1, \ldots, C_4 > 0$ (independent of L but with C_1 and C_4 monotonically depending upon M); this proves that $F_{M,L} : H \to H$. Furthermore, using the Lipschitz continuity of the functions χ_M and H_L, one can easily prove that $F_{M,L}$ is Lipschitz continuous, precisely one has

$$\begin{aligned} \|F_{M,L}(u_1) - F_{M,L}(u_2)\|_H & \leq \left(C_5 M^2 + C_6 g_{\text{syn}} M + b + \alpha L(M-1)\right)\|v_1 - v_2\|_{L^2(\Omega)} \\ & \quad + \|r_1 - r_2\|_{L^2(\Omega)} \\ & \quad + \left(g_{\text{syn}} M + g_{\text{syn}}\|v_{\text{syn}}\|_{L^2(\Omega)}) + \alpha\right)\|s_1 - s_2\|_{L^2(\Omega)}, \end{aligned}$$

for constants C_5, $C_6 > 0$ independent of M and L. For further reference, we will denote by $C_{L,M}$ the Lipschitz constant of F, i.e., it holds

$$\|F_{M,L}(u_1) - F_{M,L}(u_2)\|_H \leq C_{M,L}\|u_1 - u_2\|_H \qquad \text{for all } u_1, u_2 \in H. \qquad (4.15)$$

Let us define $u_{0,M} = (\chi_M(v_0), r, \chi_M(s_0))^T$. Then, the well-posedness of the regularized version of Problem (4.14) is assured by the following theorem.

Theorem 4.1. *Given $u_0 \in H$, $v_{syn} \in L^2(\Omega)$ and $I \in L^2(0, T_F; L^2(\Omega))$, there exists one*

and only one $u_{M,L} \in L^2(0, T_F; V) \cap C^0([0, T_F]; H)$ such that $u_{M,L}(0) = u_{0,M}$ and

$$\frac{\partial u_{M,L}}{\partial t} + A u_{M,L} = F_{M,L}(u_{M,L}) + \mathcal{I} \qquad in \ L^2(0, T_F; V') . \qquad (4.16)$$

Proof. We just give few hints for the proof. Consider the sequence φ_p, $p = 1, 2, \ldots$, of the eigenfunctions of the Laplacian operator with Dirichlet boundary conditions, which form a basis in $L^2(\Omega)$ and in $H_0^1(\Omega)$. Set $w_p = (\varphi_p, \varphi_p, \varphi_p) \in H$. For any fixed $P > 0$, let $u_{M,L}^P(x, t) = \sum_{p=1}^P \hat{u}_h(t) \varphi_h(x)$ be the solution of the Galerkin problem

$$\langle \frac{\partial u_{M,L}^P}{\partial t} + A u_{M,L}^P, v \rangle = \langle F_{M,L}(u_{M,L}^P) + \mathcal{I}, v \rangle, \qquad \text{for all } v \in V^P = \text{span}\{\varphi_1, \ldots, \varphi_P\} ;$$

let the initial condition $u_{M,L}^P(\cdot, 0)$ be the L^2-orthogonal projection of $u_{0,M}$ upon V^P. The stated problem corresponds to a system of ordinary differential equations, which admit existence and uniqueness since A is linear and $F_{M,L}$ is globally Lipschitz-continuous. In order to pass to the limit as $P \to \infty$, we observe that by difference two such solutions $u_{M,L}^P$ and $u_{M,L}^Q$ satisfy

$$\frac{1}{2} \frac{d}{dt} \| u_{M,L}^P - u_{M,L}^Q \|_H^2 + \gamma \| u_{M,L}^P - u_{M,L}^Q \|_V^2 \le C_{M,L} \| u_{M,L}^P - u_{M,L}^Q \|_H^2 ,$$

where we have used (4.13) and (4.15); hence, by Gronwall's lemma they form a Cauchy sequence in $L^2(0, T_f; V) \cap C^0([0, T_F], H)$. This guarantees the existence of a limit function, which is easily identified as a solution of (4.16). Uniqueness of this solution follows from the already invoked coercivity of A and Lipschitz-continuity of $F_{M,L}$. $\square$

4.3.3 Limit with respect to the regularization parameter M

Hereafter, we investigate the effect of letting the regularization parameter M tend to ∞. We show that under suitable assumptions on the initial data, the solution $u_{M,L}$ of Problem (4.16) is independent of M provided M is chosen large enough.

From now on, let us assume that the initial data and the applied currrent are bounded functions, precisely that $u_0 \in (L^\infty(\Omega))^3$ and $I \in L^\infty(\Omega \times (0, T_F))$. Let us first consider the third equation in (4.16), which reads

$$\frac{\partial s_{M,L}}{\partial t} = \alpha H_L(v_{M,L} - v_T)(1 - \chi_M(s_{M,L})) - \beta s_{M,L} .$$

Note that if $s_{M,L} \le 0$, then the right-hand side is ≥ 0, whence $s_{M,L}$ is non-decreasing.

On the other hand, if $M \geq 1$ and $s_{M,L} \geq M$, then

$$\alpha H_L(v_{M,L} - v_T)(1 - \chi_M(s_{M,L})) - \beta s_{M,L} \leq \alpha H_L(v_{M,L} - v_T)(1 - M) - \beta M < 0 \,,$$

whence $s_{M,L}$ is strictly decreasing. It follows that $s_{M,L}$ is bounded for all $t \geq 0$ uniformly in M and L. It follows that for M large enough, $s_{M,L}$ satisfies

$$\frac{\partial s_{M,L}}{\partial t} = \alpha H_L(v_{M,L} - v_T)(1 - s_{M,L}) - \beta s_{M,L} \,,$$

the only possible dependence on M being given by the argiment $v_{M,L}$ in the regularized Heaviside function.

In order to assess the independence on M of $v_{M,L}$ and $r_{M,L}$ for M large enough, we notice that it is enough to consider the reduced equations

$$\begin{aligned}
\frac{\partial v_{M,L}}{\partial t} &= \hat{f}(\chi_M(v_{M,L}), r_{M,L}) + I - K(\chi_M(v_{M,L}), s_{M,L}) \,, \\
\frac{\partial r_{M,L}}{\partial t} &= g(v_{M,L}, r_{M,L}) \,;
\end{aligned} \qquad (4.17)$$

indeed, the addition of the diffusive term $d^* \Delta v_{M,L}$ to the first equation does not increase the maximum positive value of $v_{M,L}$ nor decreases its minimum negative value, thanks to the Maximum Principle. (This argument can be made rigorous e.g. by considering a splitting method to advance in time the equations, in which one solves alternately the reduced equations and the heat equation in the first variable.)

We preliminary observe that $\hat{f}(v, r)$ behaves like $-v^3 - r$ for $|v|$ large enough. On the other hand, $|K(v, s_{M,L})| \leq C_7 |v| + C_8$ for any v, since we already noticed that $s_{M,L}$ is bounded uniformly with respect to M and L. Therefore, the function $\varphi(v, r) := \hat{f}(v, r) + I - K(v, s_{M,L})$ still behaves like $-v^3 - r$ for $|v|$ large enough.

Consider the vector field $\Phi(v, r) = (\varphi(v, r), g(v, r))$ in $\mathbb{R}^2$. Introducing the domain $\mathcal{D} = \{(v, r) \in \mathbb{R}^2 : |v| \leq V, |r| \leq R\}$ and carefully inspecting the behaviour of Φ on its boundary $\partial \mathcal{D}$, it is easily seen that whenever V and R are large enough, with $R < V^3$, then Φ invariably points towards the interior of $\mathcal{D}$ (see Figure 4.15; see also Example 2 at page 209 in [46] for a similar argument). This means that the dynamical system (4.17) has a positive invariant trapping region $\mathcal{D}$, so that in particular $|v_{M,L}| \leq M$ if M is large enough.

We conclude that for M large enough the solutions $u_{M,L}$ given in Theorem 4.1 are indeed independent of M, so that we can write $u_{M,L} =: u_L$. They satisfy the perturbed
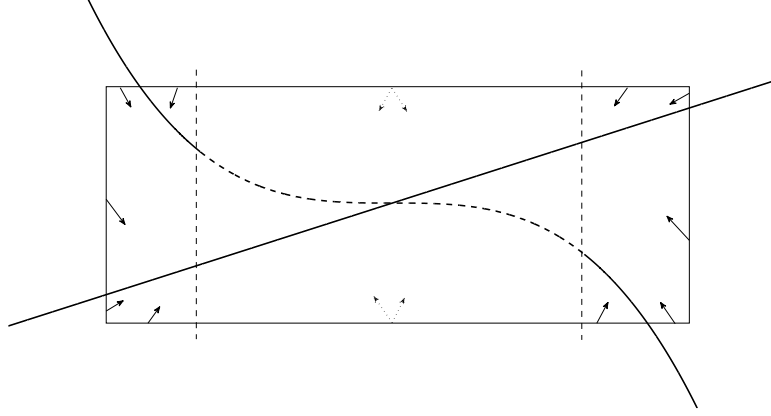
110

Figure 4.15: The phase portrait in (v, r) relative to equations (4.9). The rows describe the presence of a sufficiently large invariant rectangle

systems

$$
\begin{aligned}
\frac{\partial v_L}{\partial t} - d^* \Delta v_L &= \hat{f}(v_L, r_L) + K(v_L, s_L) + I \\
\frac{\partial r_L}{\partial t} + c r_L &= b v_L \ , \\
\frac{\partial s_L}{\partial t} + \beta s_L &= h_L(v_L, s_L) \ ,
\end{aligned}
\tag{4.18}
$$

where $h_L(v, s) := \alpha H_L(v - v_T)(1 - s)$. For further reference, we write these equations in compact form as

$$
\frac{\partial u_L}{\partial t} + A u_L = F_L(u_L) + \mathcal{I} \ ,
$$

where $F_L(u) = (\hat{f}(v, r) + K(v, s), bv, h_L(v, s))^T$.

Concerning uniqueness, it is immediate that if u_L^1 and u_L^2 are two bounded solutions of these equations with the same initial data, they also satisfy (4.16) for M large enough, hence, they coincide.

We summarize the partial results obtained so far in the following theorem.

Theorem 4.2. *Given $u_0 \in (L^\infty(\Omega))^3$, $v_{syn} \in L^2(\Omega)$ and $I \in L^\infty(\Omega \times (0, T_F))$, there exists one and only one $u_L \in L^2(0, T_F; V) \cap C^0([0, T_F]; H) \cap (L^\infty(\Omega \times (0, T_F)))^3$ such that $u_L(0) = u_0$ and*

$$
\frac{\partial u_L}{\partial t} + A u_L = F_L(u_L) + \mathcal{I} \qquad in \ L^2(0, T_F; V') \ .
\tag{4.19}
$$

Remark 3. It is easily seen that the norms of u_L in the spaces $L^2(0, T_F; V)$, $C^0([0, T_F]; H)$ and $(L^\infty(\Omega \times (0, T_F)))^3$ can be bounded independently of L. This property allows us to extract from the family $\{u_L\}$ a sequence, say u_{L_n}, that for $n \to \infty$ converges in some weak sense to a limit function u in these spaces.

Proving that such u solves equations (4.9) is a mathematically delicate matter, which hinges upon additional regularity results on the solutions u_L, uniform in L; this detailed study goes beyond the purpose of this thesis. Let us just remark that the third equation is satisfied in the sense of *differential inclusions*, namely introducing the set-valued function h^* defined in $\Omega \times (0, T_F)$ such that

$$h^*(x, t) = \begin{cases} \{0\} & \text{if } v(x, t) < v_T \,, \\ [0, 1] & \text{if } v(x, t) = v_T \,, \\ \{1\} & \text{if } v(x, t) > v_T \,, \end{cases}$$

one has

$$\frac{\partial s}{\partial t} + \beta s \in \alpha(1 - s)h^* \quad \text{a.e. in } \Omega \times (0, T_F) \,.$$

Chapter 5

Modelling multispecies networks

The set up of computer simulations describing complex networks with a huge number of nodes is a formidable challenge. The intrinsic difficulties of such a task may be handled to some extent by identifying one or more hierarchical structures within the networks; this allows one to describe and simulate several scales by exploiting different models. Within a multiscale framework, the co-existence of discrete and continuous models is a natural option, leading to significant savings. Higher-level nodes, or interactions, may be affordable given an individual description (e.g., by a system of coupled ordinary differential equations), whenever their number is small to moderate. On the contrary, this approach would be computationally prohibitive for the description of lower-level nodes or interactions, if their number is exceedingly large. In this case, a possible alternative may consist in modelling the huge cell population by a continuum, confined in some spatial region, and describing its behaviour by means of a limited number of variables, e.g., submitted to satisfy partial differential equations. One recognizes here a process underlying the mathematical description of many physical phenomena, e.g., in Fluid Dynamics.

Our multiscale approach differs from conventional ones in literature, where multiscale phenomena, in either time or space are involved in a precise manner. Regarding time, the need of a multiscale modelling is due to different time scales which are involved in many phenomena at the cellular and synaptic level. In particular, the wide interest about timescales in the neuroscientific community is due to the strict relation with the synaptic plasticity phenomenon, as presented in [11]-[23]. Regarding space, the main issue in describing different spatial areas concerns the definition of boundary conditions where the areas modelled by the microscale and the macroscale submodels interface to each other, as described in [28].

Our notion of multiscale becomes suitable to model neuronal networks involving two or more populations characterized by a high density difference; we call them multispecies networks. In order to present how to formalize such networks, we start with describing a concrete example: the Golgi-Granular cell loop network in the Cerebellum.

5.1 Golgi-Granular cell network

The Cerebellum is one of the most fascinating areas in the brain. Its description and modelling begins at the end of sixties with two outstanding researches by Marr [39] and Albus [2]. Interests on Cerebellum is due to its peculiar structure which comprehends series of highly regular, repeating units, each of which contains the same basic microcircuit. The similarity in repeating units, from architectural and physiological perspectives, implies that different regions perform similar computational operations on different inputs. These inputs originate from different parts of the brain and spinal cord projecting into the Cerebellum. In turn, the Cerebellum projects to different motor systems.

Few cellular populations are collected in this geometrically regular framework and they are located over two layers called *molecular* and *granular*. Despite the regularity of the Cerebellum facilitates his description, it remains a complex network which shows a high degree of heterogeneity among cells, and whose potentialities and functionalities are not yet fully understood.

In order to tackle the presentation and application of the multispecies modelling to a realistic network, let us focus on the Golgi-Granular cell network in the Cerebellum. We focus on this network given that it involves two populations interacting with each other with a high density difference. Notably, it is a loop network, as described in Figure 5.1, where both Granular cells (GrCs) and Golgi cells (GoCs) receive external excitatory inputs by the Mossy fibers (MFs) from other brain areas and spinal cords. Since MFs excite both cell populations, two pathways work. The first one consists in MFs exciting GrCs. These, in turn, excite GoCs through the parallel fibers (PFs), and GoCs inhibit GrCs. In a compact writing: MF-GrCs-PFs-GoCs-GrCs. The second is constituted by the excitatory input from MFs to GoCs which terminates inhibiting GrCs. This pathway is MF-GoCs-GrCs.

For our interests, the key point is that the number of GoCs highly differs from that of GrCs: GoCs are very few compared to the GrC quantity. Thus, by virtue of this high density difference, the exploitation of combined discrete and continuum models becomes reasonable. The variables described by the discrete model are relative to the single GoC
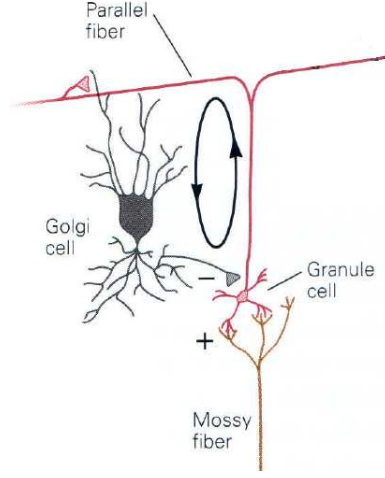
Figure 5.1: Loop involving GrCs and GoCs. External current to the system originates from MFs which synapse GrCs, as depicted, and GoCs. Furthermore, GrCs excite GoCs through PFs and, in turn, GoCs inhibit GrCs. This figure is a zoom of Figure 42-6 in [33]

i, i.e., (v_i, r_i, s_i), while the corresponding quantities in the continuum configuration, say, (ω, ρ, σ), are continuous functions in space (and time). Thus, $\omega = \omega(\xi, t)$ as well as σ and ρ.

Since each single cell in the network is modelled by the FitzHugh-Nagumo equations, it follows that the specific properties of the Golgi cells (GoCs) and of the Granular cells (GrCs) are not taken into account. In other words, they are described as excitable type II cells having features described in Chapter 1. Aware that this is a sever simplification, we refer to forthcoming works for single cell descriptions more adherent to the reality.

Inspired by assumptions in [45] and for modelling purposes, we consider the two populations belonging to two-dimensional square parallel layers, as described in Figure 5.3. The bottom one is constituted by GrC continuum and the upper one collects GoCs. A third layer, above them, collects PFs. In reality, GoC somata and GrCs are located in the just mentioned *granular layer* while the site where GoC dendrites receive input from the GrC axons (PFs) in the *molecular* one.

Let us now define the topology in the GoC-GrC network. Each GoC arborized axon reaches the granular layer throughout a cylindrical volume (whose projection on the two-dimensional granular layer is a circle), see Figure 5.2, (right). It inhibits all GrCs laying inside the circle. On the contrary, GrC axons, i.e., PFs, overcome the molecular layer and bifurcate. We suppose that PFs run parallel to the x-axis. One PF synapses onto all GoC dendrites along its path. Assuming that GoC dendrites branch out in all directions, GrC in $\bar{\xi}$ influences all GoCs in a small rectangle depicted in Figure 5.2 (left).
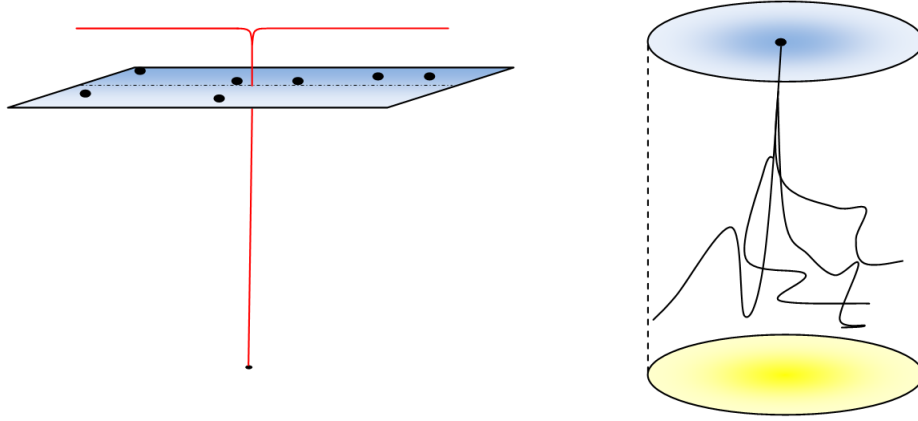
115

Figure 5.2: Connection topology between GrCs and GoGs from a presynaptic neuron perspective. Left, GrC excites through its PF all GoCs lying in the rectangle having a reasonably small height and the PF projection as the symmetry axis. Right, GoC inhibits all GrCs in the granular layer standing on a circle having a reasonable small fixed radius and the GoC projection as the center
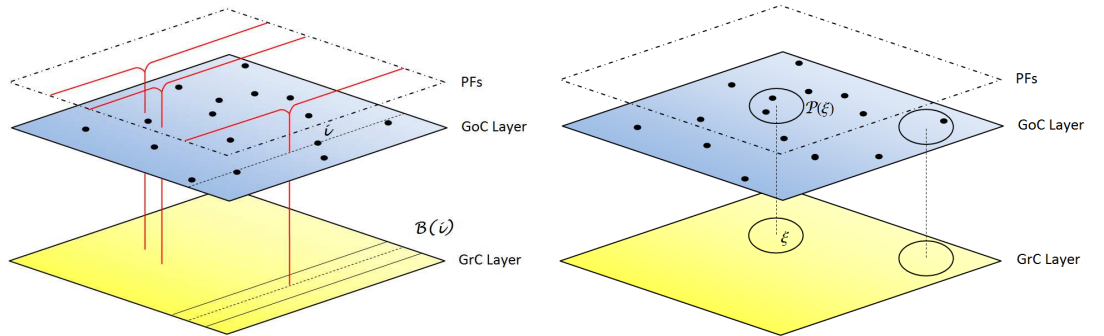

Figure 5.3: Connection topology between GrCs and GoGs from a postsynaptic neuron perspective. Left, the i GoC is excited through PFs by all GrCs in the $\mathcal{B}(i)$ rectangle. Right, GrC in $\bar{\xi}$ is inhibited by all GoCs in the upper face of an ideal cylinder having a fixed radius

Notably, GoGs receive chemical excitatory synapses by GrCs. Furthermore, GoCs are linked among each other by gap junctions.

As specified before, thanks to the high density difference between GoCs and GrCs, the latter are modelled as a continuum. The fact that GrCs constitute a continuum introduces a novelty in the coupling term for the discrete model. In order to build up the model, let us recall that all equations we used in the present work describe the postsynaptic neuron dynamics. Thus, the suitable point of view is the opposite of the one applied in Figure 5.2, and it is depicted in Figure 5.3. The whole external input term for each i-th GoC is determined as follows:

$$I_{\text{GoC},i} = d_N \sum_{j \in \mathcal{Q}(i)} (v_j - v_i) - g_{\text{syn},i} \left(\int_{\mathcal{B}(i)} \pi(i,y)\sigma(y)\,\mathrm{d}y \right) (v_i - \omega_{\text{syn}}^E) \,,$$

where the first term follows from Approach I in Chapter 2, and the integral takes into account the continuum nature of the σ variable. Another ingredient in the integral term is $\pi(i,y)$ which describes the connection weight, as explained in Chapter 3. Let us recall that, in the continuum model (3.5), the reversal potential depends upon the presynaptic neurons and, thus, it must be included in the integral term. However, since only GrCs influences GoCs by means of chemical synapses, we suppose ω_{syn}^E to be constant and we bring it out of the integral. The set $\mathcal{B}(i)$ determines the areas containing those GrCs which synapse onto the i-th Golgi cell. Taking into account that GrCs excite GoCs through the Parallel Fibers, as specified above, we consider $\mathcal{B}(i)$ as a thin rectangle whose horizontal symmetry axis is determined by the i-th cell projection. The rectangle area is chosen by fixing the rectangle height which is reasonably small.

The discrete model describing GoC dynamics has the following form:

$$\frac{\mathrm{d}v_i}{\mathrm{d}t} = f(v_i, r_i) + d \sum_{j \in \mathcal{Q}(i)} (v_j - v_i) - g_{\text{syn},i} \left(\int_{\mathcal{B}(i)} \pi(i,y)\sigma(y)\,\mathrm{d}y \right) (v_i - \omega_{\text{syn}}^E) + I_{\text{mossy},i}^{\text{GoC}} \,,$$

$$\frac{\mathrm{d}r_i}{\mathrm{d}t} = g(v_i, r_i) \,,$$

$$\frac{\mathrm{d}s_i}{\mathrm{d}t} = \alpha_i(1 - s_i)H_\infty(v_i - v_T) - \beta_i s_i \,,$$

(5.1)

where an excitatory input from Mossy Fibers, $I_{\text{mossy},i}$, is considered.

Simultaneously, the model describing the GrC continuum has to be introduced. As known from GrC literature, synapses among GrCs do not exist. However, studies in the last years claim the presence of ephaptic coupling among, in general, cortical neurons. Some references are [3, 32]; notably, the second is nowadays a fundamental

reference about this topic. The ephaptic transmission is mediated by electrical coupling between cells without specialized synapses, i.e., without the presence of a gap-junction. This kind of coupling is due to the extracellular electrical field which feeds back onto the electric potential across the neuronal membrane. It is widespread in a number of pathological situations, and so far only two clear demonstrations in healthy tissues have been highlighted: the case of the Mauthner cell and Purkinje cell, explained in [31, 32]. Despite ephaptic effects on GrCs are not yet demonstrated, we conjecture an extremely weak ephaptic transmission between GrCs due to their axonal close apposition in the cerebellar granular layer. Furthermore, concerning the coupling term between the two populations, it is well known that GrCs receive inhibitory chemical synapses from GoCs. Thus, the coupling term is

$$I_{\mathrm{GrCs}}(\xi, t) = \delta \Delta \Omega - \gamma_{\mathrm{syn}} \Big(\sum_{j \in \mathcal{P}(\xi)} p(\xi, j) s_j \Big) (\omega(\xi) - v_{\mathrm{syn}}^I) \,, \qquad (5.2)$$

where $\mathcal{P}(\xi)$ collects the GoCs which influence the GrC continuum. Since a GoC axon reaches a circular area of granular layer, centered in itself, we impose:

$$\mathcal{P}(\xi) := \{ i \in \mathbb{N} : \|x_i - \xi\| \le r_{i,\xi} \} \,. \qquad (5.3)$$

The $r_{i,\xi}$ value is chosen as reasonably small. Let us stress that, as above, the reversal potential of presynaptic GoCs is supposed to be constant and then it is not involved in the summation. By putting together all ingredients, the continuum model takes the following form:

$$\frac{\partial \omega}{\partial t}(\xi, t) = f(\omega(\xi, t), \rho(\xi, t)) + \delta \Delta \omega - \gamma_{\mathrm{syn}} \Big(\sum_{j \in \mathcal{P}(\xi)} p(\xi, j) s_j \Big) (\omega(\xi) - v_{\mathrm{syn}}^I) + I_{\mathrm{mossy}}^{\mathrm{GrCs}}(\xi) \,,$$

$$\frac{\partial \rho}{\partial t}(\xi, t) = g(\omega(\xi, t), \rho(\xi, t)) \,,$$

$$\frac{\partial \sigma}{\partial t}(\xi, t) = \alpha(1 - s(\xi, t)) H_\infty(\omega(\xi, t) - \omega_T) - \beta \sigma(\xi, t) \,.$$

$$(5.4)$$

As in the discrete model, an excitatory input from Mossy Fibers, $I_{\mathrm{mossy}}(\xi)$, is considered.

5.1.1 Numerical results

Numerical simulations have been performed with the aim of presenting how the joint models (5.1)-(5.4) work. GoCs and GrCs are collected over two squared domain whose FEM decompositions involve two different refinements. Exploiting the triangular mesh

generator BBTR, described in [6], this corresponds to set RefiningOptions parameter to 0.01 for the GoC sparse grid, and to 0.0001 for the GrC fine one. This translates into considering 94 GoCs and 7933 nodes for GrCs in the domain $[0,1]^2$. Inspired by magnitude order values in [45, 50], we set

$$g_{\text{syn},i} = 1, \quad d = 0.05 \ , \tag{5.5}$$

for the Golgi cell discrete model, and

$$\gamma_{\text{syn}} = 0.05, \quad \delta = 0.005, \quad I_{\text{mossy}}^{\text{GrC}} = 0.1 \ , \tag{5.6}$$

for the Granular cell continuous one. In particular, $I_{\text{mossy}}^{\text{GrC}}$ is applied to 10% of GrC nodes. The threshold v_T and ω_T for GoCs and GrCs, respectively, is equals to 0.5. Since cells are described by the FitzHugh-Nagumo model, it is important to recall that the threshold is not involved in the single neuron dynamics but it concerns presynaptic neuron at the synapse level. Indeed, when the presynaptic neuron overcomes the threshold, neurotransmitter release starts and influences the postsynpatic one. Let us stress that in this first simulation, only GrCs receive an excitatory input through MFs. In particular, the current is supposed to be continuous for $t > 0$. For time passing, a portrait of GoC-GrC dynamics has been obtained by exploiting (5.1)–(5.4), as shown in Figure 5.4. GoC potentials are described with bars while GrC dynamics is shown with a continuous representation. In order to make the dynamics clear, GoC potential are multiplied by a factor 3. Therefore, the reason why GoC potentials reach larger value than GrCs is simply graphical. Excitation triggered by MFs to GrCs induces an increase in GoC potentials. A subsequent inhibition in GrCs is then involved and this dynamics is reproduced with a given period. It is interesting noting that synchronous phenomena arise.

As well known, MFs input GoCs, as well as GrCs. To generate dynamics more close to reality, we consider that 10% of GoCs receive $I_{\text{mossy}}^{\text{GoC}} = 0.1$. The current is supposed to be continuous for $t > 0.5$. In the meanwhile, MF current is maintained active to 10% of GrCs from $t > 0$. The fact that continuous currents start to be injected at different time translates into an out-of-phase GoC and GrC single cell dynamics. It is worth noting that the injection of the external current to GoCs too converts the synchronous dynamics depicted in Figure 5.4 in an interesting dynamics where excitatory waves travel in the whole domain involving both GoCs and GrCs.

As mentioned before, we consider that GrCs influence each other via ephaptic coupling. It means that extracellular fields feed back onto the electric potential across
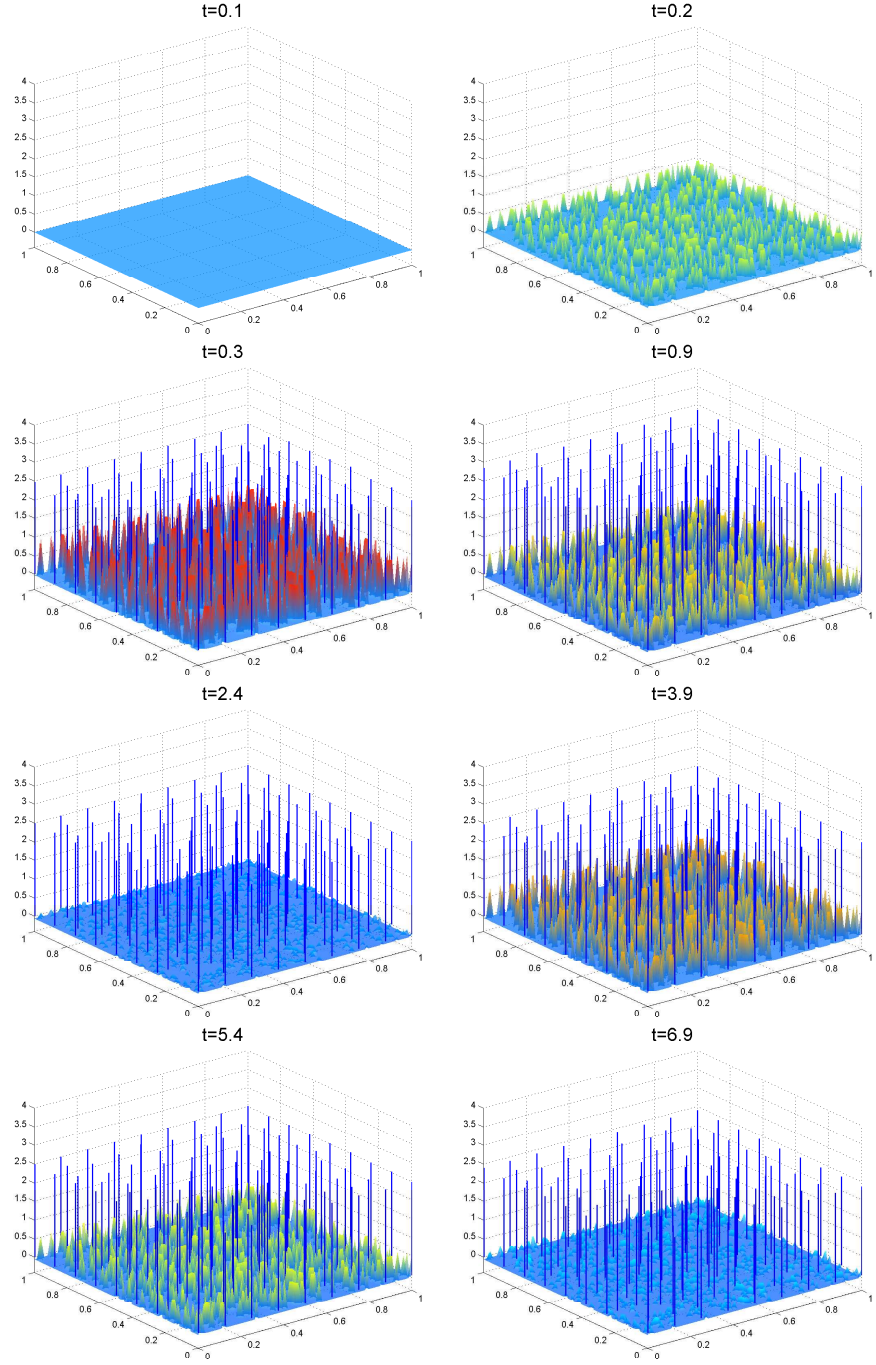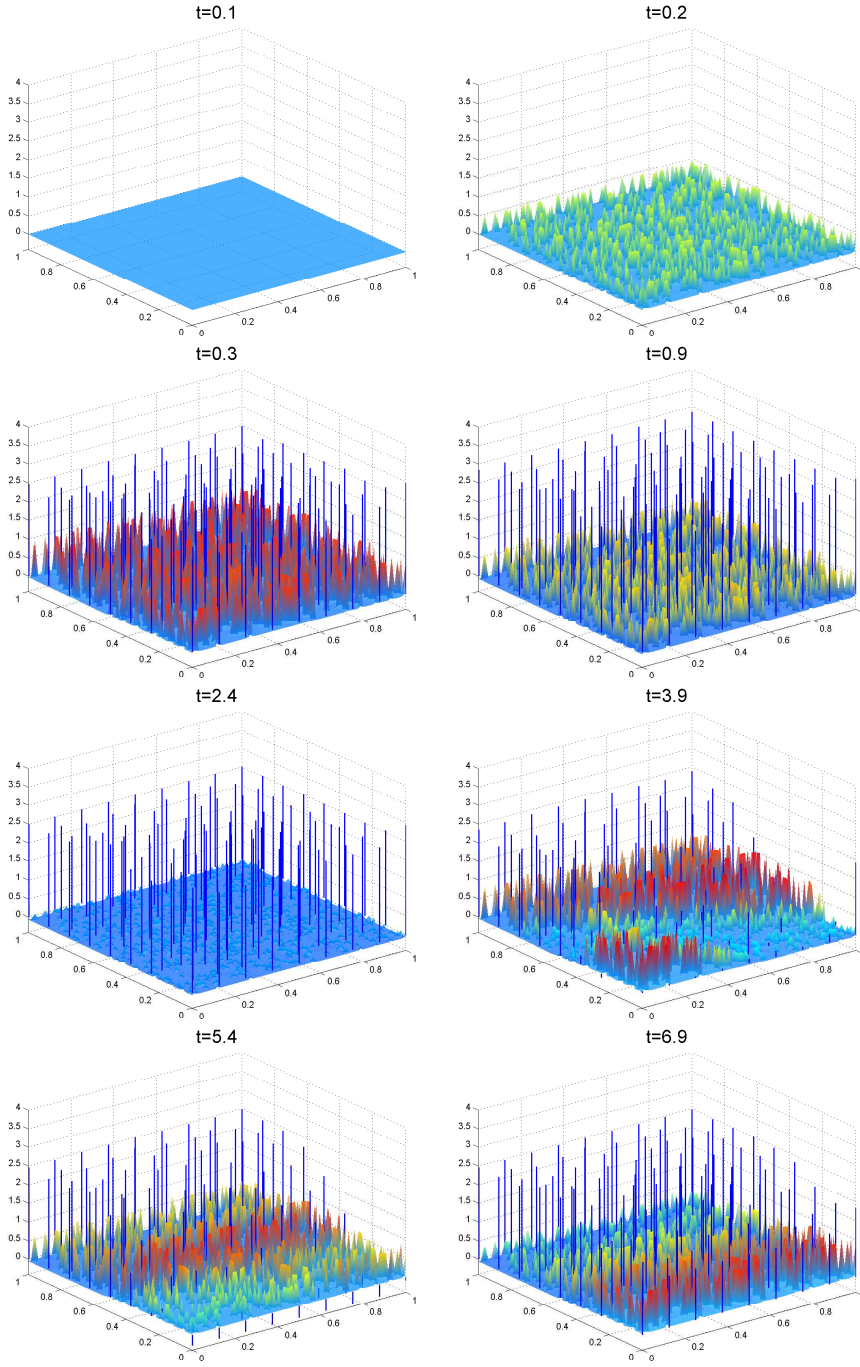
Figure 5.4: GrCs are represented with the coloured continuous graph; GoCs are described with bars showing potentials multiplied by a factor 3 for graphical reasons. A constant currents $I_{\mathrm{Mossy}}^{\mathrm{GrCs}} = 0.1$ is injected to 10% of GrCs for $t > 0$. Synchronous phenomena within each population arise. For $t > 6.9$, GoC bars return to zero and snapshots for $t \in [0.1, 6.9]$ are reproduced.

120

Figure 5.5: GrCs are represented with the coloured continuous graph; GoCs are described with bars showing potentials multiplied by a factor 3 for graphical reasons. A constant current $I_{\text{Mossy}}^{\text{GrCs}} = I_{\text{Mossy}}^{\text{GoCs}} = 0.1$ is injected to 10% of GrCs and 10% of GoCs for $t > 0$ and $t > 0.5$, respectively. By adding excitatory external input to GoCs, a travelling waves phenomena arise

121

the neuronal membranes, independent of synapses. Notably, we model this coupling as a diffusive phenomenon described in the first term of 5.2, where δ is the diffusion coefficient. Dynamics in Figures 5.4-5.5 are obtained by setting $\delta = 0.005$. In order to make clear the effect due to ephaptic coupling, let us vary the coupling strength δ. By exploiting the set up used to obtained the dynamics in Figure 5.4, in Figure 5.6 we show the evolution of membrane potential activities by considering $\delta = 0.00005$ in (a), $\delta = 0.005$ in (b) and $\delta = 0.05$ in (c). To allow the comparison with the dynamics in Figure 5.4, snapshots are taken at the same time. What we can observe is that the dynamics arisen by setting $\delta = 0.0005$ or $\delta = 0.00005$ are similar. In particular, as time passes, the excitation obtained by $\delta = 0.00005$ is more noticeable. Furthermore, by increasing the diffusion coefficient, in cases (b) and (c), we recognise a GrC lower activity. Let us stress that such excitatory reduction is in full agreement with the diffusive effect that leads to an excitation spread. Similarly, by comparing Figure 5.5 and Figure 5.7, we appreciate how much the diffusion coefficient affects dynamics when GoCs, as well as GrCs, receive MF inputs.

As δ varying, the 5.5 corresponding dynamics are collected in Figure 5.7. As in the previous comparison, we set $\delta = 0.00005$ in (a), $\delta = 0.005$ in (b) and $\delta = 0.05$ in (c). As observed before referring to the case of no MF inputs to GoCs, dynamics in Figures 5.5 and 5.7, case (a), qualitatively describe a similar phenomenon, which is characterized by travelling waves. Different behaviours arise while δ increases. Indeed, the GrC activity becomes less apparent. Nonetheless, an excitation to GoCs is provided from MFs. Thanks to this contribution, a more evident excitation in the GoC network, with respect to case (c) in 5.6, is displayed. In this configuration, the intervention of GoCs inhibition is able to elicit a rebound excitation of GrCs highlighted in Figure 5.7, case (c).

5.2 Center-surround and time-windowing

Over the recent years several studies on the GoCs-GrCs network have been focused on the analysis of how GrCs respond to both inputs they receive: the MF excitatory and the GoC inhibitory ones. In other words, the GoC inhibitory contribution modulates the excitation in GrCs triggered by MFs. It emerges from [14] that GrCs have an excitatory activity limited in space by lateral inhibition (*center-surround*) and bounded in time by feed-forward inhibition (*time-windowing*), both of them caused by GoCs.

This section is devoted to present *center-surround* and *time-windowing* noticeable phenomena reproduced by models (5.1)-(5.4). Furthermore, significant comparisons
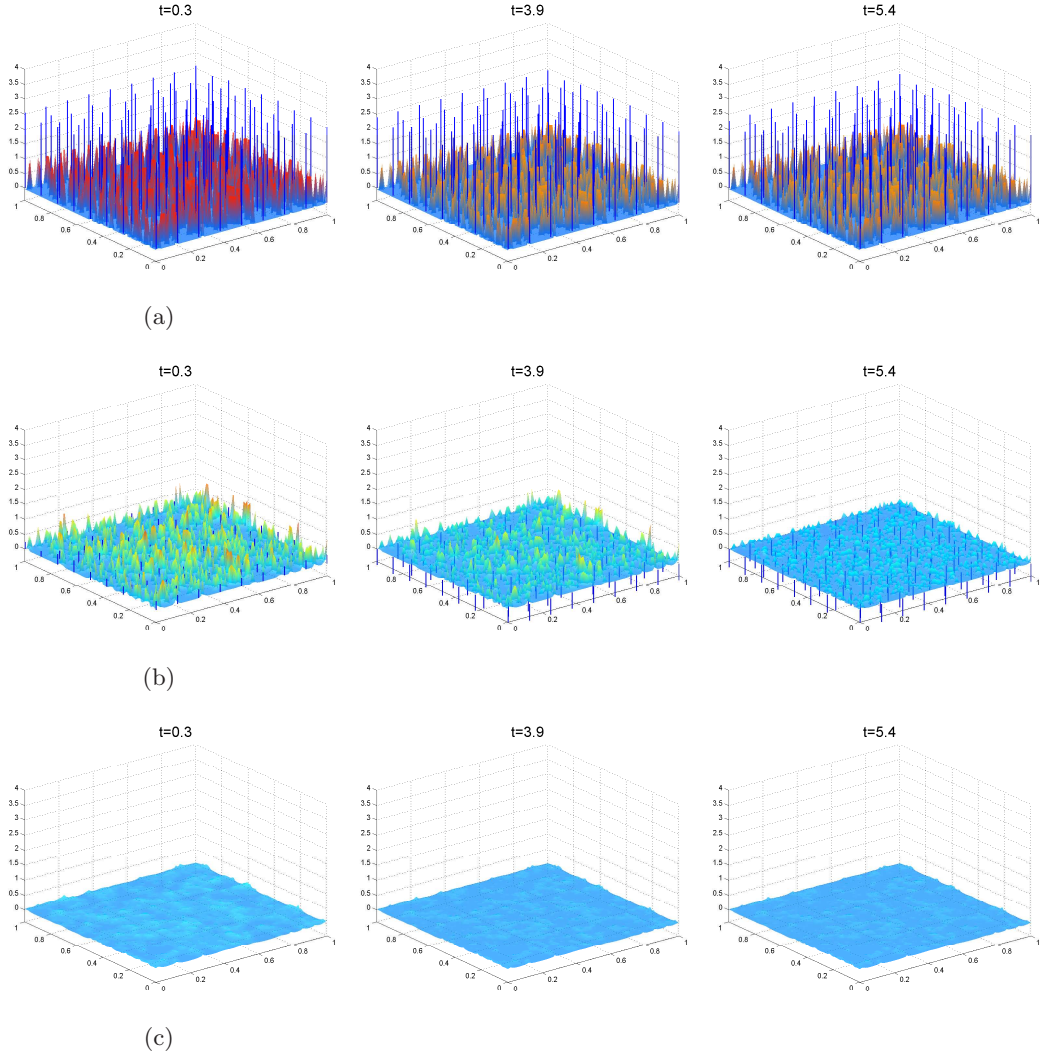
Figure 5.6: The set up used to obtain dynamics in Figure 5.4 is here exploited. Notably, diffusion coefficient δ concerning the ephaptic coupling among GrCs is set to $\delta = 0.00005$, $\delta = 0.005$, $\delta = 0.05$ in cases (a), (b), (c), respectively. A gradual reduction in GrC excitation becomes apparent as δ increases
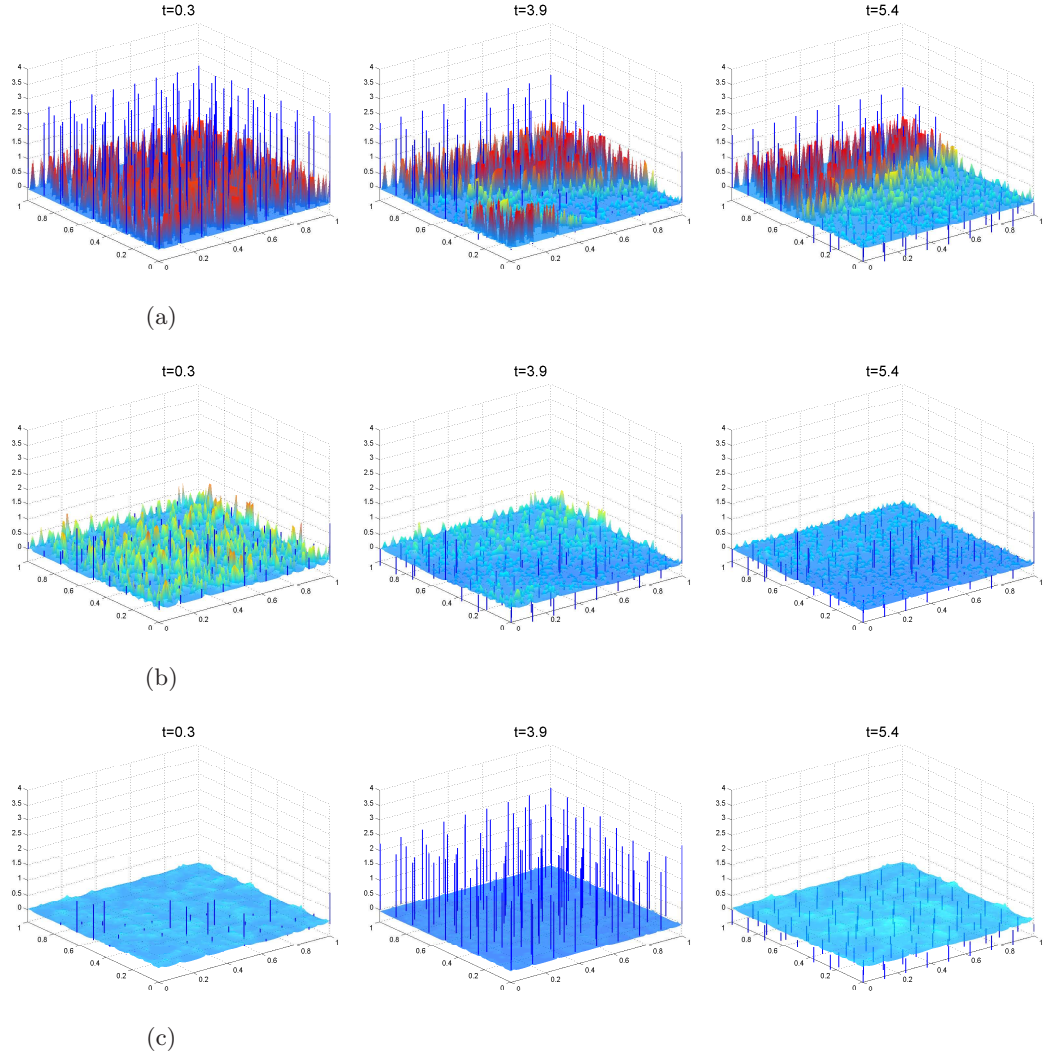
123

Figure 5.7: The set up used to obtain dynamics in Figure 5.5 is here exploited. Notably, diffusion coefficient δ concerning the ephaptic coupling among GrCs are set to $\delta = 0.00005$, $\delta = 0.005$, $\delta = 0.05$ in cases (a), (b), (c), respectively. Reductions in GrC excitation become apparent as δ increases

with results in [50] are presented. The aim of such comparisons is to stress that our models produce qualitatively similar dynamics to those shown in reference articles in the field.

In order to better reflecting the reality, we change the connection topology. Indeed, despite [2] is an eminent reference, recent studies have highlighted that GoC axons lying on a thin rectangle oriented along the sagittal axis, instead of on a circle. Notably, as specified in [7], the ratio between the rectangle's edges is 3.5.

Let us first focus on the *center-surround* phenomenon. To do this, we consider MFs exciting GrCs in a circle, having radius 1/10, located in the center of the domain, and the 5% of others in the rest of the layer. No excitatory inputs from MFs reach GoCs. On the contrary, GoCs are excited by GrCs through the PFs. In turn, each active GoC inhibits GrCs laying on a thin rectangle. Notably, we set the edge on the x axis to 1/4 while the other one has length 1.

In Figure 5.8 both GoC and GrC populations are represented. In Figure 5.9, the same dynamics is presented by zooming on the center of the domain. Snapshot times are the same as in Figure 5.8. In order to qualitatively compare our result with those in [14], let us show in Figure 5.10 two significant snapshots. The left one shows our frame at $t = 0.6$. The right one is one snapshot in Figure 5, in [50]. Let us recall that our models (5.1)-(5.4) have been subjected to severe hypotheses which do not allow us to take into account the wide variety of phenomenon in the single cell and in the whole network. Furthermore, the GrC layer has been modelled by exploiting a model reformulated as a continuum. Nonetheless, the remarkable result obtained is that our models combined together are able to reproduce the benchmark dynamics on the right, at least in the significant instant in which the *center-surround* phenomenon arises.

Concurrently, the delayed activation of GoCs allows the response of GrCs to the stimuli to survive till the GoCs inhibition arise. This configures a time window where GrCs are allowed to transfer their activity to the subsequent network layers. The intervention of GoCs inhibition closes this window resetting the GrCs activity and making them ready to reliably transmit a new stimulus.

As stressed in Chapter 1, the FitzHugh-Nagumo model describes nondimensional variables. This means that time and space scales (as well as the dependent variable values) do not reflect any biophysical-based value. In order to quantify the advantages in terms of computational costs by exploiting our model compared with others in literature, we have to evaluate our integration time in terms of a realistic time scale. We perform this by evaluating the time delay in signal transmission between two cells which belong to the Golgi and Granular populations. By analyzing simulation results, we are able
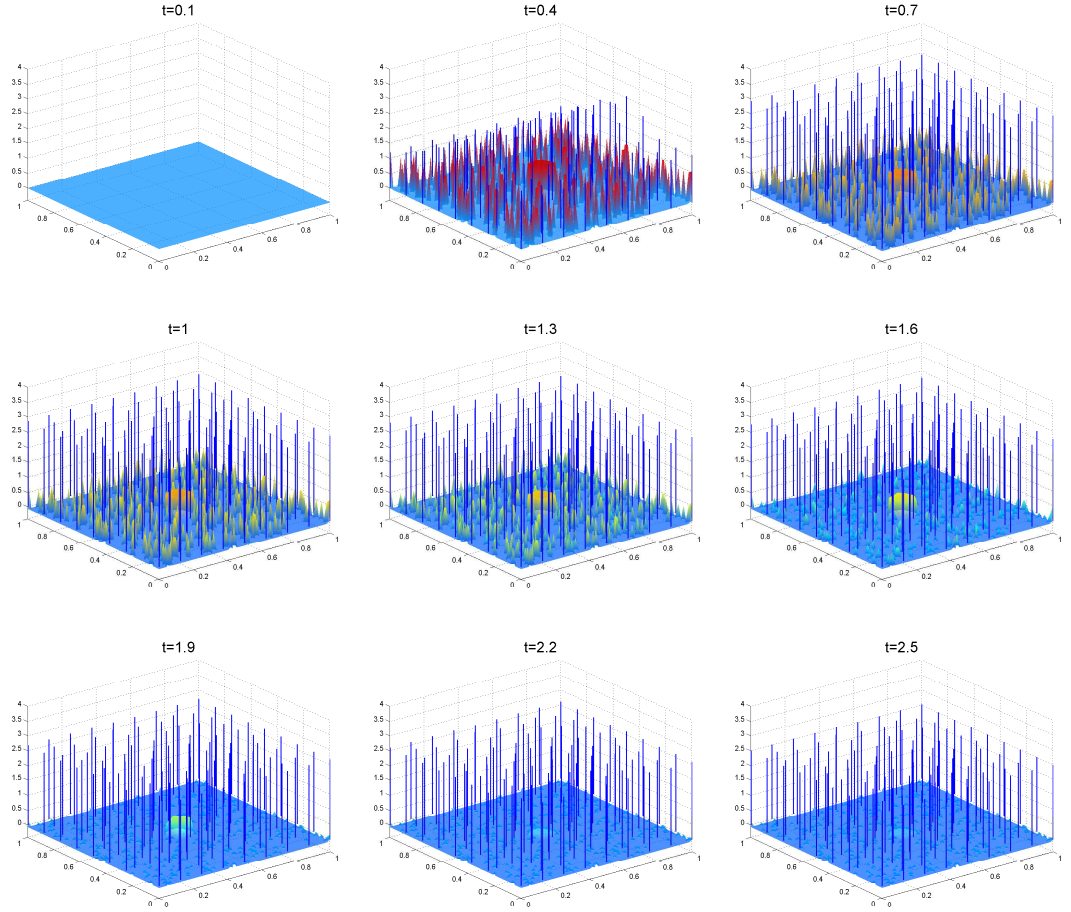
Figure 5.8: Snapshots describing center surround phenomenon in the whole domain. GrCs centered in a circle of radius 1/10 receive constant external current from MFs. GoCs, described by blue bars, receive excitation from GrCs. Each GoC inhibits, in turn, all GrCs in a small rectangle having itself as the center, the smaller edge is set to 1/4 while the bigger one has length as the whole domain. Lateral inhibition by GoCs limited in space GrC excitation. An external current to GrCs in the circle, located in the center of the domain, and to the 5% of others is injected for $t > 0$, and it continues until the simulation ends

126